Maldistribution on a Vertical Manifold With Guide Vanes

Wall-Modeled Large Eddy Simulation (WMLES) has been used to study a subsonic vertical manifolds (VMs) in terms of maldistribution, i.e., how much the flow splitting deviates from an equal flow distribution between the outlets. The analyzed configuration is characterized by a wide-angle plane diffuser and by four outlets and it has been studied at high Reynolds number ($Re^* = 10000$, with $Re^* = u_* D_h/\nu$, where u_* is the friction velocity at the inlet, $D_h = 4A/P$ is the hydraulic diameter with A the cross-sectional area at the inlet and P the perimeter, ν is the kinematic viscosity). In the basic configuration, a jet flow develops in the diffuser with two stable flow separation regions at the inclined walls, which prevent an equal flow distribution at the outlets, and determine a maldistribution around $\varepsilon = 37\%$, where ε is a parameter that quantifies the flow rate deviation from an equal distribution. To increase the equal flow distribution between the outlets, guide vanes have been used. A conceptual model to reduce the maldistribution has been developed using the momentum and the mechanical energy conservation laws. The model uses as main parameter the relative distance between the guide vanes, and it allows to minimize ε. Taking advantage of this method, the maldistribution has been reduced from $\varepsilon = 11.20\%$, for the case of equally distributed guide vanes, to $\varepsilon = 0.32\%$ in the optimized configuration. The methodology is of general use also for hydraulic systems.

1 Introduction

Uniform flow distribution is a common problem in many applications. This issue rules, for example, the exhaust flow collection from engines [1], the distribution in water supply network [2], the air distribution in HVAC system [3], it can be very important in chemical reactors [4], in the catalyst converter [5], in solar collectors [6], in heat exchangers [7] and so on. Generally, in pipe systems, the arrangement for the flow distribution (or collection) is defined as a manifold. Its main scope is to split the flow rate from a main channel to different branches, or if it works in the opposite way, its role is to merge the flow from several inlet into a common outlet. The first case is defined as a diverging manifold, while the second one as a combining manifold. Considering the diverging manifold class, a key point is to guarantee an equal flow distribution between the different outlets. The flow splitting is often associated with a pressure recovery, which in the end prevents the equal distribution. This phenomenon is called maldistribution.

Over the years, different strategies have been adopted to study the manifold: first laboratory experiments have been carried out and successively the analysis has been conducted using analytical model, discrete model, or computational fluid dynamics (CFD). A seminal work is that of Ref. [8], where an analytical model, based on momentum balance, has been used. This approach has been extended by [9], with a simplified procedure for the manifold's analysis, based on the solution of two equations: a pressure-flow equation and a flow distribution equation. A further development is by [10] to include frictional effects. For discrete model see among the others [11]. When using CFD, manifolds are generally investigated by taking advantage of the Reynolds-averaged Navier–Stokes equations (RANS), see for example, [12], and for the turbulence modeling see Ref. [13]. For a general introduction to the theory of manifolds see Ref. [14].

Most of the analysis has been done on the consecutive manifold configuration, where a main header is associated with a set of lateral parallel branches. On the other hand, other arrangements are relevant, see for example, [15]. For example, other manifolds are based on flow bifurcation, with a tree-shaped structure, and with the inlet aligned with the outlets, see for example, Refs. [16] and [17]. These configurations allow a better equal flow distribution, but with a strong drawback related to the space requirement, which prevents its practical applicability. Within the same concept, a particular type of diverging manifold is that of Fig. 1(*a*), this arrangement is characterized by an inlet aligned with the outlets, in this sense, we talk about a vertical manifolds (VMs), and the flow distribution is performed through a diffuser. In some way, this configuration resembles a Penstock bifurcation or trifurcation, and it is common in industrial drying hood, in catalyst converter (see Refs. [1,5,18]), in chemical reactors (see Ref. [19]), in plate-fin heat exchanger (see Ref. [20]).

In a classical consecutive diverging manifold, the key element for the flow distribution analysis is the T-junction, in the VM this role is taken by the diffuser. Its geometrical characteristics, together with the inlet flow condition, rule the distribution.

For a planar diffuser, where the wall expansion angle acts only in one direction, the most important geometrical aspects are: the diffuser wall expansion angle ϕ, the characteristic lengths ratio N/W_1, where N is the diffuser extension, while W_1 is the inlet width, and the aspect ratio $AR = W_2/W_1$, where W_2 is the width at the diffuser exit, see Fig. 1(*b*). In this configuration, the fluid dynamics is characterized by different flow regimes, in terms of flow separation at the walls. If the Reynolds number ($Re = UD_h/\nu$ with U the mean inlet velocity, D_h the hydraulic diameter, and ν the cinematic viscosity) is sufficiently high, larger than 5×10^4 ([21]), these flow regimes depend only on the geometrical aspects, ϕ or W_2/W_1 versus N/W_1, [22]. For example, consider the case where the lengths ratio N/W_1 is maintained constant, while the diffuser angle ϕ varies:

(1) A first regime is obtained for small angles. The flow from the inlet, going into the diffuser, remains attached to the walls and there are no appreciable flow separation regions if time-mean is considered, while, instantaneously flow separation can occur.
(2) Increasing the angle, a second regime takes place. The flow in the diffuser is characterized by the presence of a large transitory flow separation region, which alternatively forms at the two expansion's walls. When these structures detach, they have transported away in the flow field. With a further

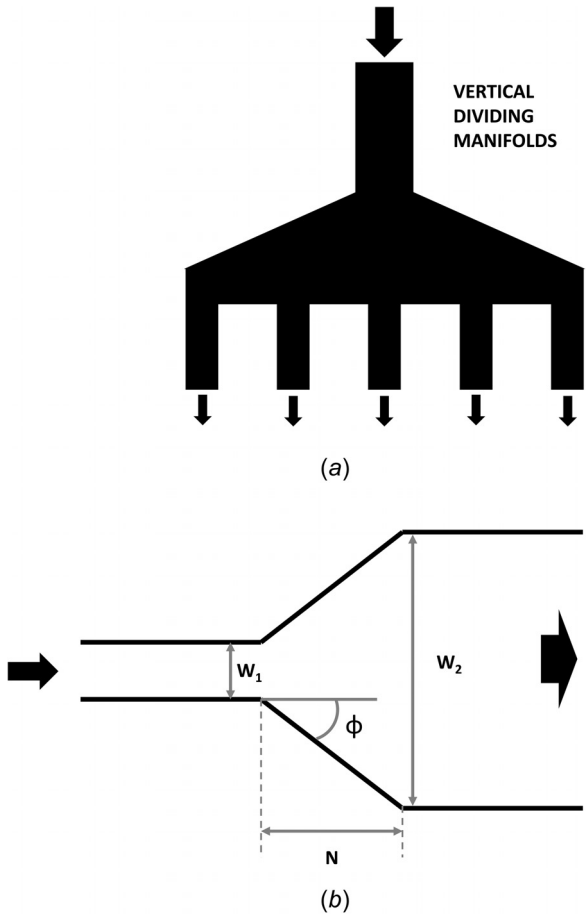

Fig. 1 (*a*) Sketch of a vertical diverging manifold and (*b*) planar diffuser geometrical aspects

increase of the angle, the flow separation region may be quasi-stable, it develops only on one side of the diffuser and it can persist for a long time in this condition without detaching.

(3) For an even larger angle value, the flow from the inlet to the diffuser behaves like a jet, two large stable flow separation regions are present at the diffuser walls, this is the third regime. This last condition is typical for the so-called wide diffuser.

For a better description of these flow regimes see Ref. [23] and its famous chart.

If, for example, we have the ratio AR = 3, a value of $N = 60W_1$ is required to obtain a small angle ϕ and to be in the first regime of no appreciable flow separation condition. This configuration is desirable because it reduces the local head loss and it guarantees a better flow uniformity at the diffuser exit. On the other hand, the extension of the diffuser, related to N, can be an issue. Indeed, in a number of situations, this solution cannot be implemented because of space restrictions. In real applications, the wide diffuser is the rule, not the exception, typical values are in the range from $N/W_1 = 1.5$ and AR > 2.5, to $N/W_1 = 10$ and AR > 30. Once a wide planar diffuser is used in a VM, stable flow separation regions develop at the diffuser walls, interacting with the outlet channels, and consequently, a strong maldistribution condition is expected. Several strategies can be used to improve the flow uniformity at the diffuser exit. The key point is to prevent flow separation formation. A simple solution is to use screens (or perforated plates, or cylinder arrays) inside the diffuser. The flow is forced to pass through a grid, which increases turbulent mixing, and forces momentum transfer from the streamwise to the transverse directions, see among the other [24–26]. The main disadvantage is that the screen introduces a strong head loss. Another solution, which avoids increasing the head loss, is to use guiding vanes at the diffuser inlet, see for example, [27]. Other strategies could be implemented (flow suction, artificial roughness, cavities, vortex generator, threshold, etc., see for example, [28–30]), but in most applications, this is considered the only practical method to improve flow distribution in a wide planar diffuser ([31]). The guiding vanes can also extend for the entire diffuser length. In this case, the diffuser can be considered as divided into several subdiffuser with a smaller characteristic expansion angle. The use of guide vanes results in an increase in the continuous head loss due to the additional walls, but overall the head loss is reduced if the flow separation regions disappear or are strongly reduced. This can be obtained using an optimum number of vanes, which is strictly connected to the diffuser expansion angle, for example, in the range $60\,\text{deg} < 2\phi < 90\,\text{deg}$ is 6, see Ref. [27].

If a wide planar diffuser is associated with a VM, it could be reasonable to use a number of guide vanes directly associated with the number of outlets. Within this work we want to analyze a VM characterized by a planar wide diffuser, where guide vanes are used to create smaller diffusers, directly connected to the outlets. Then we address the following questions:

(1) how much beneficial is the use of guide vanes in a VM in terms of the maldistribution?
(2) which strategies can be adopted for the guide vanes position in the inlet channel to reduce maldistribution?

The study is carried out using both an analytical method and a numerical one. First, the VM configuration will be analyzed in terms of characteristic control volumes, where the conservation law for momentum, for mass and the energy equations will be applied. As a result, a strategy to avoid maldistribution will be derived. This approach will be later used to define the configurations to be studied numerically through CFD, in this case we take advantage of Wall-Modeled Large Eddy Simulations (WMLES), solving the filtered version of the Navier–Stokes equations. In WMLES the large energy carrying turbulent scales are directly resolved, while the smallest ones, below the grid cell size, are modeled through a subgrid scale model (SGS). Moreover, to reduce the computational cost, the viscous sublayer is not directly solved and its effect is provided to the interior flow with a wall function, see Ref. [32]. The WMLES, although computationally expensive, is used because it is able to reproduce unsteadiness and three-dimensional features hardly reproduced by standard RANS computations. In a wide diffuser, the flow separation regions are mainly fixed, but once subdiffusers with a reduced angle are introduced, transitional flow separation could appear, see for example, [33]. Unsteady Reynolds-averaged Navier–Stokes (URANS) model can be unable to reproduce these phenomena, see Ref. [34].

The paper is structured in the following way: in Sec. 2 an analytical model is proposed together with the cases under investigation; the governing equations, for the numerical simulations, are described in Sec. 3; the boundary conditions for the test cases are in Sec. 4; results are in Sec. 5; finally, the conclusions are in Sec. 6.

2 Analytic Model and Test Cases

A sketch of the geometry for the manifold herein considered is in Fig. 2(*a*), only a plane xz is shown, considering that the expansion angle ϕ does not act in the y direction. Along the flow direction (from left to right in Fig. 2(*a*)) the system is composed of four main elements: an inlet duct, a diffuser, a mixing area, and several outlet channels. The first element is a square channel with a side dimension W_1, and an extension of $4W_1$, to avoid reflection toward the inlet condition. The diffuser has a length of $N = 1.5W_1$ and a total wall expansion angle $2\phi = 70\,\text{deg}$. With these geometrical aspects the diffuser belongs to the wide-diffuser category and in the case of high Reynolds number the jet regime is expected. Between the diffuser and the outlet channel an area

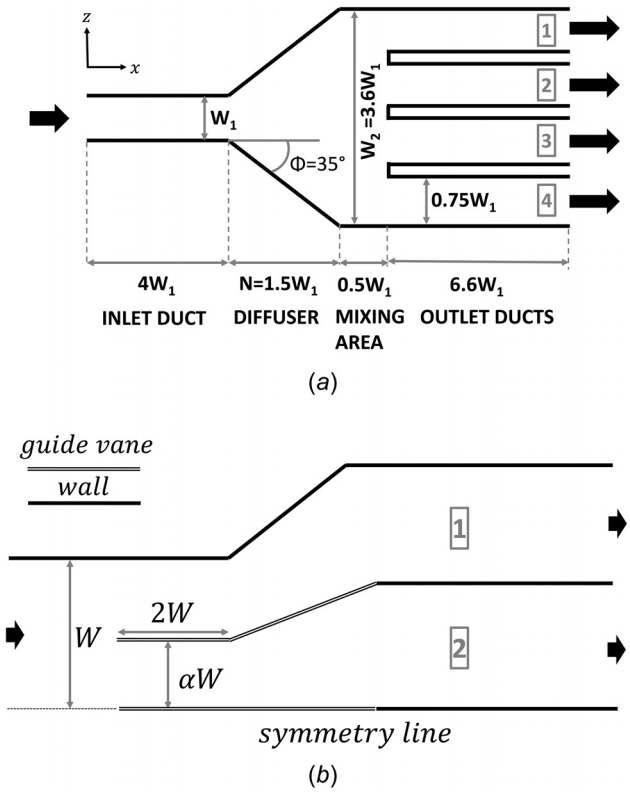

Fig. 2 (*a*) Sketch of the vertical manifold and its characteristic dimensions and (*b*) planar guide vanes arrangement and geometrical aspects

with extension $0.5W_1$ is considered. Generally, this area should be longer, because it is beneficial to allow a channel flow profile recast. Here it is considered small, in the view of the space restriction issue, related to the use of a wide diffuser, and then to highlight the possible maldistribution. Finally, there are four outlet ducts with width of $0.75W_1$ and with an extension of $6.6W_1$ to avoid possible interaction between the entrance effects and the domain outlet.

The geometry of Fig. 2(*a*) is considered as the initial case (*C0*). The other configurations have the presence of the guide vanes, these extend for W_1 inside the main channel and are connected to the outlet channels. The total number of guide vanes is three, one along the symmetry plane of the diffuser, the other two are symmetrical with respect to the central one, see Fig. 2(*b*), where only half of the manifolds are shown. The positions of these two external guides is defined in terms of αW (where $W = 0.5W_1$ is half of the inlet channel height), the distance from the symmetry plane, where $0 < \alpha < 1$. To analyze the manifold, we first consider the flow rate Q^*. It is defined as the target value to have an equal flow distribution at the outlet, therefore, $Q^* = Q_{\text{in}}/N_{\text{out}}$, where Q_{in} is the flow rate at the inlet and N_{out} the number of outlet channels. In the present case $Q_{\text{in}} = 4Q^*$.

Consider the scheme of Fig. 3, where only half of the manifolds are shown, with respect to a plane of symmetry. The presence of the external guide vane, splits the right part of the geometry into two channels, channel 1 is the external and resembles an s-bend configuration; channel 2 is closer to the symmetry line and is characterized by an asymmetric diffuser. Within half of the manifold the inlet flow rate will be $2Q^*$. The generic flow rate measured at the outlet can be declined in terms of Q^*, as $Q^* + \varepsilon Q^*$, where ε is a number, $-1 < \varepsilon < 1$, which represents a maldistribution parameter. If $Q^* + \varepsilon Q^*$ flows through channel 2, by continuity, $Q^* - \varepsilon Q^*$ flows through the channel 1. Now, to analyze the behavior of the manifold, we defined two characteristic sections: section A is taken in the main duct, upstream, far from the guide vanes, in a location where the inlet channel flow can be considered unaffected by the presence of the guide vanes; section B is taken exactly at the origin of the guide vanes. If we draw an imaginary line, from section A to section B, at the height of the guide vane, it divides the inlet channel into two control volumes, see Fig. 3. The inflow flow rate can be declined in terms of Q^*, so $Q^* + \delta Q^*$ flows through section with area A_2, and $Q^* - \delta Q^*$ through the section with area A_1, where δ is a number, $-1 < \delta < 1$.

Looking at the control volume 2 of Fig. 4(*a*), by continuity, a flow rate is required to pass between section A and section B, through the imaginary line. This flow rate will be function of δ, ε. There will be a transfer of momentum to the streamwise direction, associated with this cross flow and to its velocity component V_x along the streamwise direction. So, there will be a loss of momentum in the control volume, if the flow rate is going out from it, and a gain of momentum if the flow rate is going into the control volume. Table 1 shows the possible contribution with its sign for the control volume 2.

Figure 4(*b*) shows a scheme of the momentum and the forces acting on the control volume 2, this extends also in the y direction till the walls. By applying the momentum conservation on the control volumes 1 and 2, we obtain

$$A_1(P_{A_1} - P_{B_1}) - 2WL\tau_{12} - 2WL\tau_{wz} - (1-\alpha)WL\tau_{wy} = \rho\left[\frac{(Q^* - \varepsilon Q^*)^2}{A_1} - \frac{(Q^* - \delta Q^*)^2}{A_1} + FV_xQ^*\right] \quad (1)$$

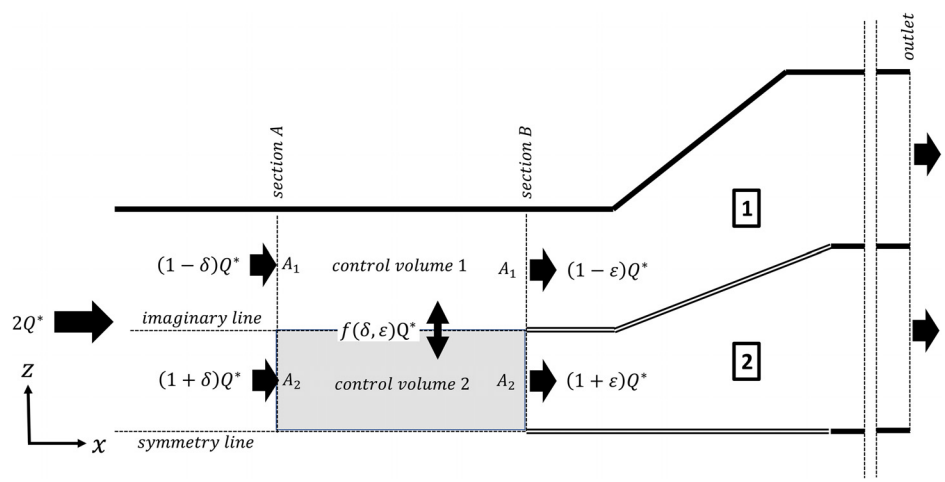

Fig. 3 Sections and control volumes definition for half manifold

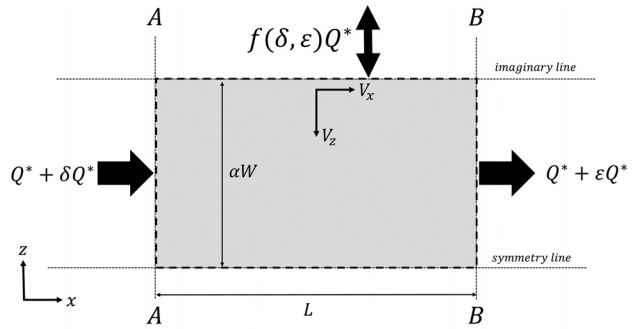

(a)

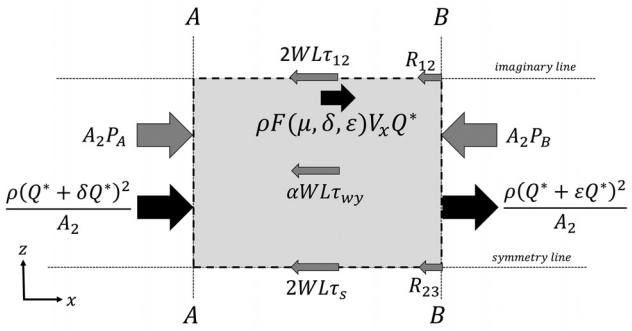

(b)

Fig. 4 Control volume 2: (*a*) flow rates at the boundaries and (*b*) forces acting on the control volume

Table 1 Possible cases of flow rate through the imaginary line and the associated momentum for control volume 2

Case	Flow rate	Direction	Momentum	μ_δ	μ_ε
$\delta>\varepsilon>0$	$(\delta-\varepsilon)Q^*$	out	$\rho(\varepsilon-\delta)V_xQ^*$	0	0
$\delta=\varepsilon>0$	0	—	$\rho(\varepsilon-\delta)V_xQ^*$	0	0
$\varepsilon>\delta>=0$	$(\varepsilon-\delta)Q^*$	in	$\rho(\varepsilon-\delta)V_xQ^*$	0	0
$\delta>0;\varepsilon<0$	$(\delta+\varepsilon)Q^*$	out	$-\rho(\varepsilon+\delta)V_xQ^*$	0	1
$\delta<0;\varepsilon>0$	$(\delta+\varepsilon)Q^*$	in	$\rho(\varepsilon+\delta)V_xQ^*$	1	0
$\delta<\varepsilon<=0$	$(\varepsilon-\delta)Q^*$	in	$\rho(\varepsilon-\delta)V_xQ^*$	0	0
$\delta=\varepsilon<0$	0	–	$\rho(\varepsilon-\delta)V_xQ^*$	0	0
$\varepsilon<\delta<0$	$(\delta-\varepsilon)Q^*$	out	$\rho(\varepsilon-\delta)V_xQ^*$	0	0

$$A_2(P_{A_2}-P_{B_2})-2WL\tau_{12}-2WL\tau_s-\alpha WL\tau_{wy}=\rho\left[\frac{(Q^*+\varepsilon Q^*)^2}{A_2}-\frac{(Q^*+\delta Q^*)^2}{A_2}-FV_xQ^*\right] \quad (2)$$

where the reaction R from the guide vane has not been taken into account, considering that the guide vane width is small compared to the control volume and it faces the flow with a rounded profile. In the equations, P is pressure, L is the length of the control volume in the streamwise direction, A is the cross area, ρ is density, τ_{12} is the stress along the imaginary line, τ_{wz} and τ_{wy} are the wall stresses in direction z and y, τ_s is the stress along the symmetry line (therefore $\tau_s=0$), the indices 1 and 2 refer to the control volume. The term F quantifies the momentum transfer to the streamwise direction between the two control volumes, because of the flow rate through the imaginary line, so it takes opposite sign in the two equations, its form is

$$F=\rho[(2\mu_\delta-1)\delta+(1-2\mu_\varepsilon)\varepsilon] \quad (3)$$

The term $\mu_{\delta,\varepsilon}$ is a number with value 0 or 1, the term F represents all the possible cases as described in Table 1. Subtracting Eq. (1) from Eq. (2), the following relation is obtained

$$P_{B_1}-P_{B_2}=\frac{\rho}{A_2}\left[\frac{(Q^*+\varepsilon Q^*)^2}{A_2}-\frac{(Q^*+\delta Q^*)^2}{A_2}-FV_xQ^*\right]-\frac{\rho}{A_1}\left[\frac{(Q^*-\varepsilon Q^*)^2}{A_1}-\frac{(Q^*-\delta Q^*)^2}{A_1}+FV_xQ^*\right] \quad (4)$$

Section A is far from the guide vanes, in an undisturbed position, and we have assumed $P_{A_1}=P_{A_2}$, then we have considered that the differences between the stresses are negligible, this choice has been adopted for example, in Ref. [8]. Equation (4) shows how the pressure difference at the inlet of the two channels is a function of the momentum transfer characterizing the two control volumes in front of the guide vanes and the flow rates.

Now, we consider the mechanical energy equations between section B and the outlet for the channels 1 and 2. In the present study, there is no a mechanical work due, for example, to a pump. External heat transfer has not been considered. The gravity vector is considered acting on the y direction (in case of liquid). Furthermore, working with an incompressible flow, we assume that pressure and temperature do not affect the density, so the thermal terms are dropped out except for that related to friction. Then the mechanical energy equation reduces to

$$\frac{P_{B_1}}{\rho}+a\frac{(Q^*-\varepsilon Q^*)^n}{2A_1^n}=\frac{P_{\text{out}}}{\rho}+a\frac{(Q^*-\varepsilon Q^*)^n}{2A_{\text{out}}^n}+k_1a\frac{(Q^*-\varepsilon Q^*)^n}{2A_{\text{out}}^n} \quad (5)$$

$$\frac{P_{B_2}}{\rho}+a\frac{(Q^*+\varepsilon Q^*)^n}{2A_2^n}=\frac{P_{\text{out}}}{\rho}+a\frac{(Q^*+\varepsilon Q^*)^n}{2A_{\text{out}}^n}+k_2a\frac{(Q^*+\varepsilon Q^*)^n}{2A_{\text{out}}^n} \quad (6)$$

Here the subscript out refers to the outlet section, and we have considered that the outlet sections for the channels 1 and 2 are equal; k_1 and k_2 are the head loss coefficients which take into account both the local and the continuous head loss; a is the Coriolis parameter and n the exponent for the kinetic term. At section B, the velocity profile is related to an incoming well-developed pipe flow; the outlet sections are at a distance larger than $5D_h$ from the diffuser, sufficient to have a recast to a well developed velocity profile because of turbulent mixing, for these reasons a is set equal to one. Moreover, the high Reynolds number considered allows to set $n=2$. Subtracting Eq. (6) from Eq. (5)

$$P_{B_1}-P_{B_2}=\rho\left(\frac{1+k_1}{2A_{\text{out}}^2}-\frac{1}{2A_1^2}\right)(Q^*-\varepsilon Q^*)^2-\rho\left(\frac{1+k_2}{2A_{\text{out}}^2}-\frac{1}{2A_2^2}\right)(Q^*+\varepsilon Q^*)^2 \quad (7)$$

Equation (7) shows how the pressure difference at the inlet of the two channels is a function of the head loss coefficients, of the flow rates and of the areas. Combining Eqs. (4) and (7), allows to drop out the pressure terms, and after a rearrangement, we obtain a quadratic equation in ε

$$\psi\varepsilon^2-2\xi\varepsilon+\eta=0 \quad (8)$$

where the terms are

$$\psi=\frac{k_1-k_2}{2A_{\text{out}}^2}+\frac{1}{2A_1^2}-\frac{1}{2A_2^2} \quad (9)$$

$$\xi=\frac{2+k_1+k_2}{2A_{\text{out}}^2}+\frac{1}{2A_1^2}+\frac{1}{2A_2^2}-\left(\frac{1}{A_1}+\frac{1}{A_2}\right)(1-2\mu_\varepsilon)\frac{V_x}{Q^*} \quad (10)$$

$$\eta = \psi + \frac{(1+\delta)^2}{A_2^2} - \frac{(1-\delta)^2}{A_1^2} + 2\left(\frac{1}{A_1} + \frac{1}{A_2}\right)\frac{V_x}{Q^*}(2\mu_\delta - 1)\delta \tag{11}$$

Equation 8 allows understanding the maldistribution not only for the values of k_1 and k_2, but also as a function of the position of the guide vane, and the associated momentum transfer before the diffuser. The equation should be used to understand when the modulus of ε has a minimum. In Ref. [35], a maldistribution parameter has been explicitly computed through a model based on the energy equation, for a flow between parallel microchannels. For this case, a direct solution was possible, because the authors considered a laminar flow, the head loss coefficients were not unknown and the transverse velocity (before the parallel channel) was set to a prescribed value. In the present case, the computation of ε would require the knowledge of the head loss coefficients, which in the end are also function of the guide vanes position, and cannot be estimated a priori. Nevertheless, Eq. (8) provides useful information. Indeed, a possible condition to have a minimum for ε, is when $\eta = 0$, and $\varepsilon = 0$ is a solution for Eq. (8), which means from Eq. (11)

$$\psi + \frac{(1+\delta)^2}{A_2^2} - \frac{(1-\delta)^2}{A_1^2} + 2\left(\frac{1}{A_1} + \frac{1}{A_2}\right)\frac{V_x}{Q^*}(2\mu_\delta - 1)\delta = 0 \tag{12}$$

And expanding the terms of Eq. (12)

$$\frac{k_1 - k_2}{2A_{\text{out}}^2} = \frac{(1-\delta)^2}{A_1^2} - \frac{1}{2A_1^2} - \frac{(1+\delta)^2}{A_2^2} + \frac{1}{2A_2^2} - 2\left(\frac{1}{A_1} + \frac{1}{A_2}\right)\frac{V_x}{Q^*}\delta \tag{13}$$

On the left-hand side (LHS), we have collected the difference between the two head loss coefficients k_1 and k_2. The right-hand side (RHS) is a function of the areas A_1 and A_2, of δ and V_x, while $\mu_\delta = 0$, because $\varepsilon = 0$ is associated with Eq. (13), see Table 1.

Analyzing the terms on the RHS, it can be observed that the area A_1 and A_2 can be expressed as a function of α, with $A_1 = 2(1-\alpha)W^2$ and $A_2 = 2\alpha W^2$.

The split term δ is also a function of α. Fig. 5(*a*) shows, for a turbulent square channel flow at $Re^* = 10000$, how δ varies in terms of α (see the solid line). It can be observed that, for a large range of α, the behavior is linear (see the dashed line). At high Reynolds number flow, because of turbulent mixing, the mean velocity profile, in the core region, tends to be flat, and this is reflected by the linear behavior of δ. As α tends to 1, the velocity profile is affected by the wall friction and δ deviates from the linear behavior. When δ is linear it assumes the form $\delta = c\alpha - b$, with c the angular coefficient and b the intercept. α^* is the value giving $\delta = 0$.

Finally, an evaluation of the term V_x is required; we can consider that its value is related to the streamwise velocity at the interface between the two control volumes. This velocity varies between the section A and the section B. At the section A, by definition, the flow is undisturbed and we can consider a velocity scale of the form $(Q^* + \delta Q^*)/2\alpha W^2$, i.e., the mean velocity crossing section A_2, at section B there will be a stagnation point because of the guide vane, so the streamwise velocity tends to zero as the guide vane is approached. If we assume a linear behavior between the two sections, then a characteristic velocity scale for the momentum transfer could be $V_{x,\text{mean}} = (Q^* + \delta Q^*)/4\alpha W^2$.

Substituting the above relations, Eq. (13) can be expressed in terms of α as

$$\frac{A_A^2}{2A_{\text{out}}^2}(k_1 - k_2) = \frac{3\alpha - 2}{(1-\alpha)^2\alpha^2}(c\alpha - b)^2 - \frac{4\alpha^2 - 5\alpha + 3}{(1-\alpha)^2\alpha^2}(c\alpha - b) + \frac{2\alpha - 1}{2(1-\alpha)^2\alpha^2} \tag{14}$$

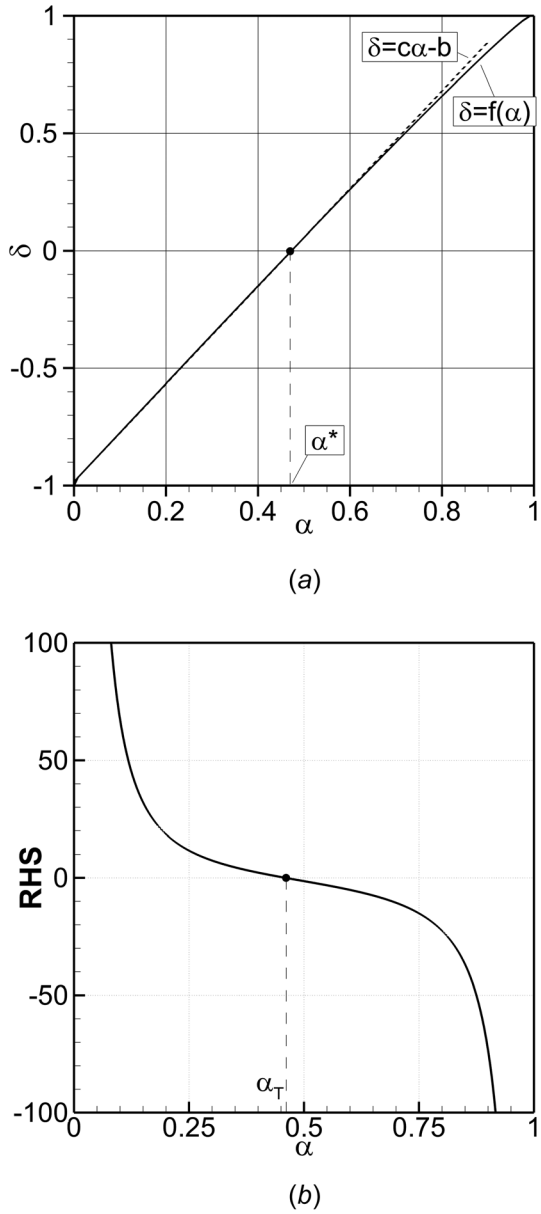

Fig. 5 Channel flow with square section at *Re=10000: (*a*) δ in terms of α, solid line, linear assumption for δ, dashed line and (*b*) RHS as a function of α**

where A_A is half of the total inlet area. Equation 14 relates the difference between the head loss coefficient to the α parameter. Without knowing the value of K_1 and K_2, the equation still provides useful information, if it is declined in terms of the sign of the difference between k_1 and k_2. If $k_1 > k_2$ then it must be RHS > 0, if $k_1 < k_2$ it implies RHS < 0. Fig. 5(*b*) shows the behavior of RHS(α) considering the inlet condition that will be later adopted in the simulations, with $c = 2.0798$ and $b = 0.983$ for the linear assumption on δ. The RHS goes to +-infinite as α tends to 0 or to 1, respectively, and it has a zero value at $\alpha_T = 0.461 < \alpha^*$. This trend is reasonable and intuitive. Assume that the guide vane is located at half of the midchannel, $\alpha = 0.5$, and k_1 is much greater than k_2, then most of the flow rate would pass through channel 2 with respect to channel 1, to compensate this trend α should be moved toward the 0, to increase the transfer of momentum from channel 2 to channel 1. Then the RHS must be positive as α tends to zero, and negative if α tends to 1.

The limit case of $\alpha = 1$ corresponds to a configuration where the flow cannot pass through channel 1, because of the guide vane

position. In this case it would be $\varepsilon_1 = -1$ and $\varepsilon_2 = 1$, very far from the equal flow distribution condition $\varepsilon = 0$. Therefore the condition $\eta = 0$ should not be satisfied. If $\alpha = 1$, then the RHS $= -\infty$, see Fig. 5(*b*). The condition of zero flow through channel 1 can be associated with $k_1 = +\infty$, while k_2 has a finite value, then LHS $= +\infty$. Therefore, the LHS and the RHS have opposite infinite values, Eq. (14) is not satisfied and we cannot expect $\varepsilon = 0$. The same reasoning applies to the case $\alpha = 0$, but with opposite values.

From these limiting cases, we can derive another relevant statement, as α goes from zero to one, the LHS goes from $-\infty$ to $+\infty$, while the RHS goes from $+\infty$ to $-\infty$, then there must be at least one intersection between these two functions, and therefore a condition $\eta = 0$ exists.

The LHS of Eq. (14), as mentioned, is not known a priori, but it can be computed numerically. Then for a specific α, if the LHS is equal or close to the analytical RHS, ε should be close to zero, i.e., an equal flow distribution. After these considerations, the test cases, solved numerically, in terms of the guide vane position, are chosen according to Table 2.

Case 0 ($C0$) is the case without guide vanes. It allows to highlight the maldistribution. The other cases use the guide vanes. Case 1 ($C1$) has $\alpha = 0.5$. It means that a uniform distribution of the guide vanes is considered in the inlet channel. This configuration is the one suggested by [27]. Case 2 ($C2$) has $\alpha \simeq \alpha^*$. In this case the parameter α is chosen such that $\delta = 0$. Case 3 ($C3$) has $\alpha < \alpha_T$. Finally, case 4 ($C4$) is with α much lower than α_T. These cases allow to define a trend for the head loss coefficient difference $k_1 - k_2$. Then, a final case, defined from the intersection between the RHS and LHS behavior, will be run.

As a final note, the above method could be declined for an arbitrary number of outlets, introducing for each branch i the parameters δ_i and ε_i and the additional equations

$$\sum \delta_i = 0; \quad \sum \varepsilon_i = 0 \tag{15}$$

3 The Numerical Model

The test cases are analyzed numerically, solving the filtered version of the Navier Stokes equations, namely, the mass and momentum conservation which read as

$$\frac{\partial \overline{u_i}}{\partial x_i} = 0 \tag{16}$$

$$\frac{\partial \overline{u_i}}{\partial t} + \frac{\partial \overline{u_j}\,\overline{u_i}}{\partial x_j} = -\frac{1}{\rho}\frac{\partial \overline{P}}{\partial x_i} + \frac{\partial}{\partial x_j}\nu\frac{\partial \overline{u_i}}{\partial x_j} - \frac{\partial \tau_{ij}}{\partial x_j} + D \tag{17}$$

where the overbar means filtered quantities, u_i is the velocity component in the x_i direction; and directions 1, 2 and 3 correspond to x, y, and z in a cartesian frame of reference. P is the hydrodynamic pressure, D is a bodyforce acting on the flow (for example, gravity), τ_{ij} is the sub-grid scale (SGS) momentum fluxes. This element derives from the filtering operation, and it represents the flow contribution of the unresolved scales, while the large, anisotropic and energy-carrying scales of turbulence are directly solved.

Table 2 Simulation cases

Case	α	Condition
$C0$	—	—
$C1$	0.500	$\alpha > \alpha^* > \alpha_T$
$C2$	0.468	$\alpha \simeq \alpha^* > \alpha_T$
$C3$	0.452	$\alpha < \alpha_T < \alpha^*$
$C4$	0.404	$\alpha < \alpha_T < \alpha^*$

The SGS term is modeled with an eddy viscosity approach based on the equilibrium assumption

$$\tau_{ij} = -2\nu_t \overline{S_{ij}} \tag{18}$$

where ν_t is the eddy viscosity and S_{ij} is the large-scale strain rate tensor equals to

$$\overline{S_{ij}} = \frac{1}{2}\left(\frac{\partial \overline{u_i}}{\partial x_j} + \frac{\partial \overline{u_j}}{\partial x_i}\right) \tag{19}$$

Finally, the eddy viscosity is computed as

$$\nu_t = c_s \Delta^2 |\overline{S}| \tag{20}$$

where c_s is the Smagorinsky constant, set to 0.85, Δ is the filter width, relate to the grid through the Deardorff length scale, $\Delta = (dxdydz)^{1/3}$, where dx, dy, dz are the cell length in the three directions, $|S|$ is the strain rate contraction.

The governing equations are solved numerically on a structured grid with collocated variables. The algorithm is a fractional step method as in Ref. [36]. The Poisson equation to force continuity is solved with a SOR method with a V-cycle multigrid accelerator.

The solver is second-order accurate both in space and in time. The time advancement is performed semi-implicitly with an explicit Adams-Bashfort scheme for all the terms except the diagonal diffusive ones, where a Crank-Nichols implicit scheme is used. Finite differences are used for space derivatives, particularly the convective term is solved with a third-order cubista scheme, [37]. The analysis is carried on with a structured cartesian grid, an immersed boundary method (IBM) is used to deal with the geometrical characteristics of the manifolds, see Fig. 6 for a sketch. The employed IBM belongs to the direct-forcing approach as in Refs. [38] and [39], and the boundary effect is considered in Eq. (17) through the term D. For a general review on the approach see Ref. [40].

The computational domain has dimensions $L_x = 12.60W_1$, $L_y = 1.0342W_1$ and $L_z = 3.6198W_1$, and it is discretized with 280 cells in the streamwise direction, 128 in the y direction and 448 in the z direction, with a total of approximately 16 million cells, around 6.5 million belong to the solid phase of the immersed boundary.

The mesh size has been defined accordingly to the wall model requirements, see Ref. [41], and to avoid an excessive cell aspect ratio, see Ref. [42]. Therefore, the grid cells are constant everywhere with $\Delta y^+ = \Delta z^+ = 80.8$, (in terms of wall unit $y^+ = yu^*/\nu$), while $\Delta x^+ = 404$, except in the outlet channels

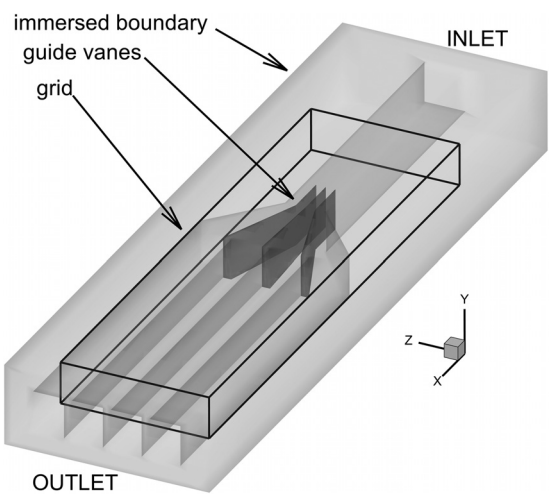

Fig. 6 Domain sketch

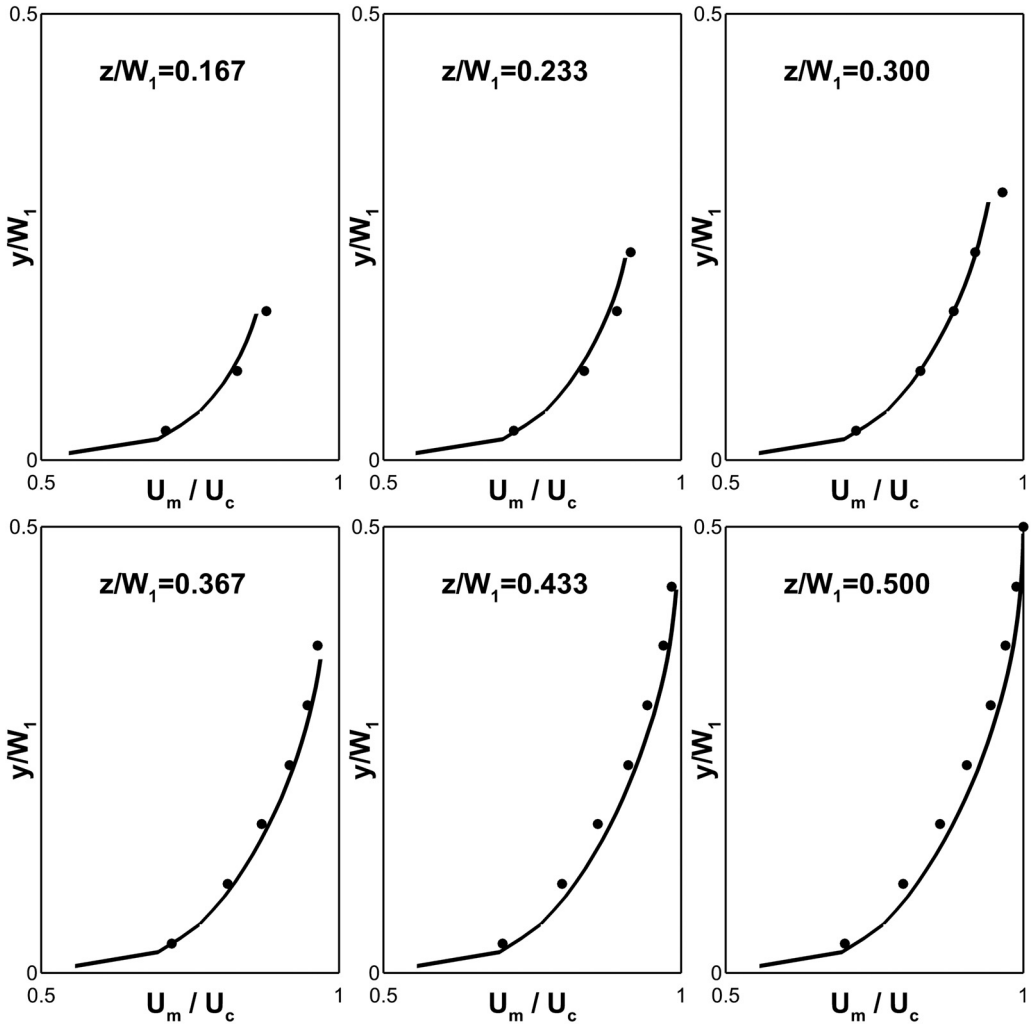

Fig. 7 Mean streamwise velocity scaled with the mean centerline velocity, comparison at different location in the *z* direction, solid line represent WMLES solution, black circles are from the experimental results of Ref. [48]

where a 1% stretching is used for the streamwise direction to guarantee a longer outlet section and to avoid to cut the stable separation areas developed from the diffuser.

In terms of the length scale W_1, the grid sizes are $\Delta y = \Delta z = 0.00808W_1$ and $\Delta x = 0.0404W_1$. The inlet channel in both y and z direction is solved with 126 fluid cells, in the subchannels, defined from the guide vanes and the inlet duct, the z resolution is between 28 and 32 cells, therefore with a resolution often employed in large eddy simulation with wall function, see Refs. [43–46], and it allows to solve the boundary layer, see Ref. [47].

4 Boundary Conditions

At the domain inlet, a turbulent velocity profile with coherent evolving structure is required, otherwise LES is not able to sustain turbulent production. This issue is solved by considering a prerun simulation of a periodic duct flow, driven by an imposed pressure gradient. At each time-step, a cross-sectional plane yz of variables has been stored, and then it has been provided as a prescribed inflow condition at the inlet of the manifolds. The prerun simulation has the same grid resolution of the manifold inlet duct, to avoid interpolation errors, the streamwise length is $3.5W_1$, with sides of length W_1. This periodic square channel has been run with $Re^* = 10000$, where Re^* is based on the friction velocity u^* as velocity scale and the hydraulic radius as length scale. Before running this simulation, the model has been tested at $Re^* = 3860$, and the results have been compared with experimental data of Ref. [48]. Figure 7 shows the results from LES with wall modeling for the mean streamwise velocity (scaled with the centerline mean velocity U_c) along y direction at different locations along the z direction, compared with the experimental results. The comparison looks satisfactory. The reference paper reports the following ratios $U_c/U_b = 1.2$ and $u^*/U_b = 0.47$ (where U_b is the bulk velocity), while the WMLES simulation has 1.184 and 0.0478, respectively.

Less satisfactory results, but still acceptable, are obtained for the turbulent fluctuations. Figure 8 shows the root-mean-square (rms) values for velocity at different locations. The peak in the experimental data for the streamwise component is well reproduced by WMLES, then the numerical simulation provides information closer to the wall and therefore higher peaks are observed. Overall the WMLES results are lower than the experimental results, in Ref. [48] the quantities v_{rms} and w_{rms} are reported to be computed with lower accuracy with respect to the other turbulent quantities. On the other hand, the general behavior is reproduced, at the location $z/W_1 = y/W_1 = 0.5$ (the square duct center) an isotropic behavior is observed as expected. Maintaining the y location and moving along lower values of z/W_1, the turbulent structures reflect the wall influence, an anisotropic behavior is observed for both the numerical and the experimental results, with v_{rms} and w_{rms} values lower than u_{rms}.

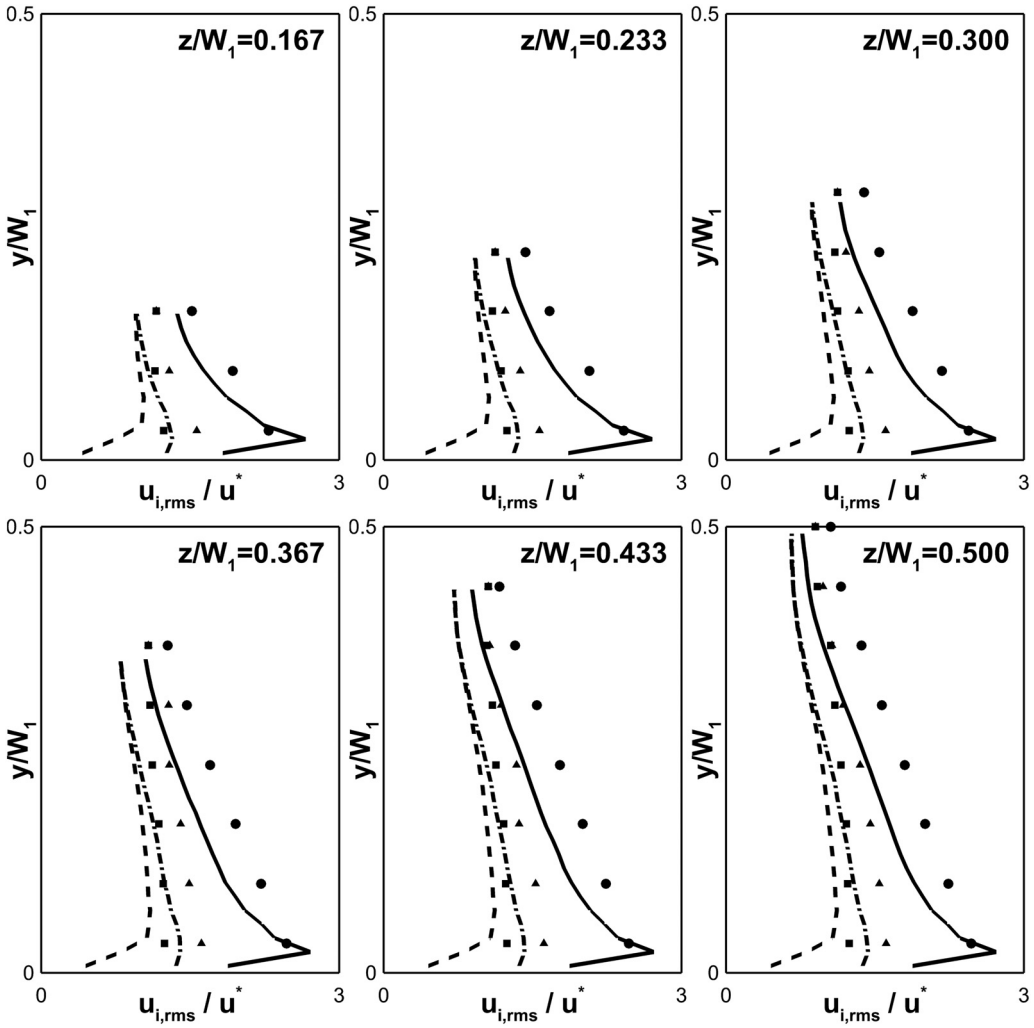

Fig. 8 Turbulent fluctuations intensities in terms of rms scaled with the friction velocity comparison at different location in the *z* direction: solid line, dash dot, and dash line represents u_{rms}, v_{rms}, w_{rms} WMLES solution, black circles, triangles and squares are u_{rms}, v_{rms}, w_{rms} from the experimental results of Ref. [48]

At the outlet an Orlanski condition is applied, [49]. It means that a purely convective equation is solved at the boundary. To avoid reflection from the outlet inside the domain, the equation is solved with a dissipative first-order upwind scheme.

At the wall, considering the Reynolds number, a wall function is applied, this means that the viscous layer is not directly solved, to avoid an excessive computational cost. In the context of the immersed boundary, the standard wall model approach cannot be used, because the grid and the wall do not coincide, therefore, we use the specific method of Ref. [45], which is based on a velocity reconstruction from the interior flow field at the first off-wall node and on a local increase of the eddy viscosity derived form a mixing length procedure; where flow separation occurs a linear scheme is used to interpolate the velocity field at the interface between the fluid and solid zone. The present model takes advantage of the analyzed configuration: the large wall expansion angle induces a strong adverse pressure gradient, moreover, the presence of a sharp corner, between the inlet duct and the diffuser, triggers flow separation. In the case of small expansion angles, with mild or weak adverse pressure gradient, a proper model would require considering the dependency on the pressure gradient.

5 Results

Figure 9 shows an instantaneous contour plot for the streamwise velocity u, made nondimensional with the inlet friction velocity u_*, at a section $y/W = 1$ for the manifolds in the initial configuration, so without the guide vanes. Fig. 9 refers to a time before the steady-state condition is reached. With LES also the transitional phase has a physical meaning, and figure allows to understand the interaction between the flow separation regions and the outlets.

As expected, the flow from the inlet channel, as it goes into the diffuser, behaves like a jet, and two strong stable recirculation regions develop at the inclined wall. The diffuser angle is so high that its throat can be considered as a discontinuity for the flow, so we are not in the case of smooth surface transition. These flow separation structures start immediately downstream of the throat, span over the entire diffuser and also in the short area of mixing, and they strongly interact with the outlet channels, especially the channel 1 and 4. The flow separation regions maintain the flow from the inlet channel confined into the core of the diffuser. This has a strong impact on the flow distribution. As the simulation reaches a steady-state, the flow separations areas have ruled the flow dynamic, see Fig. 10, where a contour for the mean streamwise velocity is shown. The samples for the statistical procedure have been collected for a total time of $133.6T$ (where $T = 0.5W_1/U_c$ is an inertial time scale related to the boundary layer thickness at the inlet channel $0.5W_1$). Then, averaging has been performed with respect to the axis of symmetry.

The flow separation regions, shown in Fig. 9, determine a backflow at the outlet 1 and 4, which in the end behave like an

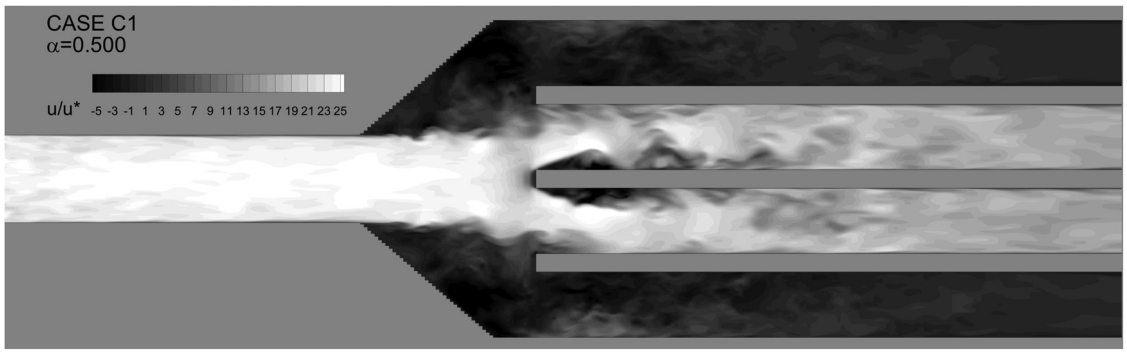

Fig. 9 Contour for the instantaneous streamwise velocity component *u* for the base configuration, case *C*0, before a steady-state condition

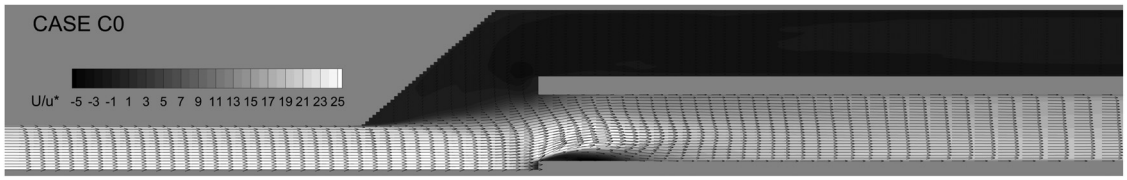

Fig. 10 Velocity vectors and contour for the mean streamwise velocity component U for the case *C*0. For the sake of clarity only one vector every 16 is shown.

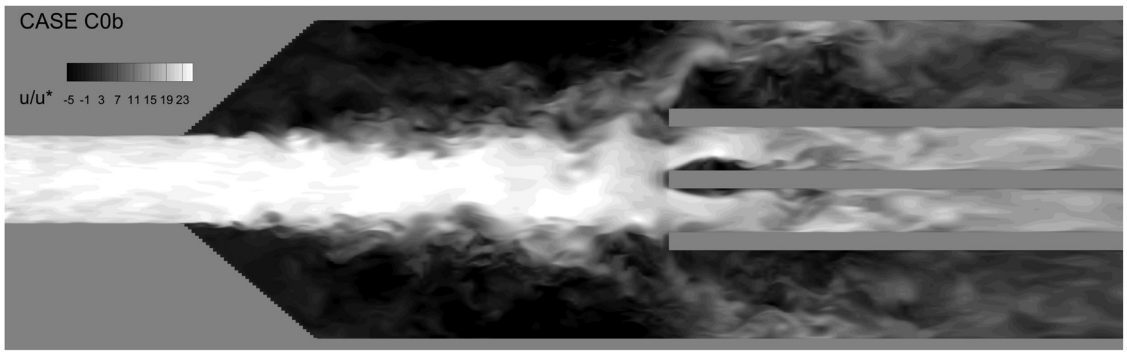

Fig. 11 Contour for the instantaneous streamwise velocity component *u* for the base configuration, case *C*0b

additional inlet, for a similar behavior see Ref. [50]. Therefore, the incoming flow from the inlet flows into the interior channels, 2 and 3, and the maldistribution coefficient has a value greater than one.

To improve the performance of the manifolds, without adding the guide vanes, two strategies can be implemented: first, the width of the outlet channels can be increased, in this way the head loss is reduced, moreover, the larger cross-sectional area avoid to have a complete obstruction from the flow separation region; secondary, the mixing area can be extended to allow a better recast to a uniform flow by turbulent mixing.

To prove the benefits of these solutions, an additional simulation, *C*0*b*, has been run increasing the outlets areas for channels 1 and 4 ($A_{\text{out},1,4} = W_1^2$ and $A_{\text{out},2,3} = 0.5W_1^2$) and with a mixing area of $4W_1$. For this case the streamwise number of cells has been increased to 336. Figure 11 shows a contour for the instantaneous streamwise velocity, when a steady-state condition is reached. The flow separation regions in the diffuser are clearly detected, moreover strong entrance effects are visible at the beginning of the outlet channels, especially for the exterior ones. With this configuration the exterior channels behave as outlet, still the maldistribution is relevant, with an average value of 37%. Although there is an improvement, the obtained maldistribution justifies the use of different solutions, like the guide vanes.

Figure 12 shows a contour plot at $y/W = 1$ for the instantaneous streamwise velocity for case $C1$, with $\alpha = 0.5$, so the configuration suggested in Ref. [27]. As already mentioned, with this configuration the diffuser is divided into subdiffuser elements, directly connected to the outlets. The subdiffuser connected to channels 2 and 3 resembles an asymmetric diffuser, while for the channels 1 and 4 a turning diffuser, with something like an" s" configuration. The guide vanes start in the inlet channel, allowing a better split of the flow rate and reducing the impact on the flow of the two stable regions observed for the case $C0$. At the beginning of the guide vanes, flow separations associated with entrance effects are not observed. This is related to the fact that the guide vanes face the streamwise flow with a rounded profile to reduce the drag. Qualitatively, from Fig. 12, it can be seen that the outlets channels are characterized by a better flow distribution. Still separation areas are observed in the subdiffusers, especially at the walls with a higher inclination, but also at the exit from the subdiffuser for channel 1 and 4.

For case $C1$, the samples for statistics are collected for the same time window as case $C0$, because of the presence of the guide vanes, an inertial time scale of the type $T_{\text{diffuser}} = 0.5h(x,\alpha)/U_b$ can be defined, where h is the height of the subdiffuser and it varies as a function of the x coordinate and of α, see Ref. [33]. For channel 2, we have $\Delta T = 534T_{\text{diffuser,inlet}}$ and

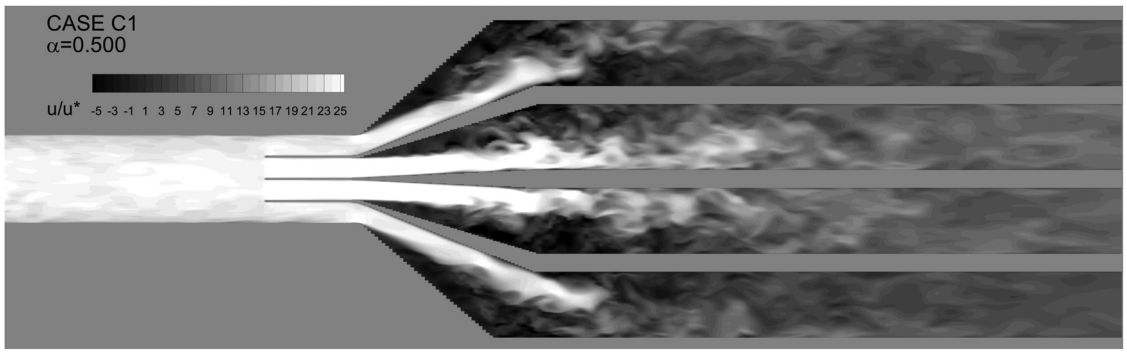

Fig. 12 Contour for the instantaneous streamwise velocity component *u* for the case *C*1, at a steady-state condition

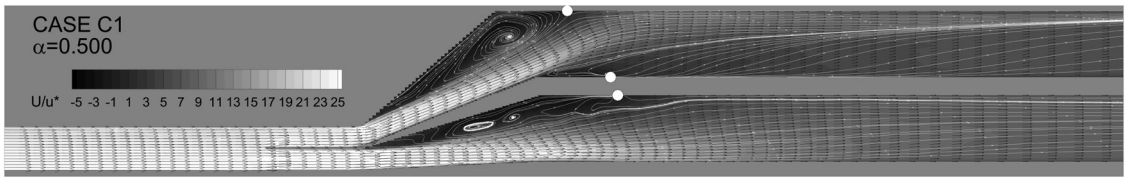

Fig. 13 Streamlines, velocity vectors, and contour for the mean streamwise velocity component U for the case *C*1. The circles correspond to the point with $\tau_{wall} = 0$. For the sake of clarity only one vector every 16 is shown.

$\Delta T = 59T_{\text{diffuser,outlet}}$, where $T_{\text{diffuser,inlet}}$ is computed at $x = 3W_1$, the subdiffuser inlet, and $T_{\text{diffuser,outlet}}$ is computed at $x = 6W_1$, the subdiffuser outlet. This last time scale is larger than that at the inlet, because U_b is reduced at the subdiffuser outlet. The simulated cases show the presence of stable separation zones, therefore the flow is characterized mainly by high-frequency structures, related to the shear effect between the reverse flow areas and the through flow, while low-frequency structures, associated with transitional separation areas, are not observed. For this reason, and for the results obtained (later described) the time window seems adequate.

The stable separation areas can be better appreciated by looking at Fig. 13, where a contour plot for the mean streamwise velocity is shown at $y/W = 1$. The white circles show the point where the first off-wall velocity changes the sign, and provide an indication about flow reattachment and where the wall stress is going to zero. The flow separation areas have a longer extension for the interior channels 2 and 3 with respect to the exterior channel 1 and 4. Indeed, for channels 1 and 4, the S-shape configuration brings the main flow to be pushed against the outer wall, allowing a confinement of the separation into the subdiffuser.

Figure 14 shows the instantaneous value of ε, computed for each one of the outlets, in a time range of 133.6 T, after the steady-state condition is reached. The values are quite constant in time, except for very small variations due to the evolution of turbulent structures and of the separation zones, as previously described. With respect to the base configuration, the maldistribution between the outlets has been strongly reduced, with an average value of $\varepsilon = 11.2\%$. A greater flow rate is observed in the interior channels 2 and 3, and accordingly, a lower value in the exterior channels 1 and 4 (negative value of ε). Although the system behavior has remarkably improved with respect to the base configuration, still the maldistribution cannot be considered satisfactory.

In terms of the flow field, the simulations $C2$, $C3$, and $C4$ show similar behavior with respect to $C1$, as it can be seen for the mean streamwise velocity from Figs. 15(*a*), 15(*b*), and 15(*c*). For these cases the inertial time scales, related to the subdiffuser, are of the same order of magnitude of case $C1$. As α is reduced, $T_{\text{diffuser,inlet}}$ decreases and $T_{\text{diffuser,outlet}}$ increases. In all the analyzed cases the area of the flow separation appears in a stable way at the most inclined walls. Within the considered range for α, the flow reattachment positions are similar between the cases, see Table 3, only for the case $C4$, with the lower value of α, the reattachment point for channel 2 and 3 is further downstream, on the other hand, this behavior is consistent with the increase of the aspect ratio for the axisymmetric diffuser, indeed separation increases as a function of the Reynolds number [51] and of the diffuser angle [52].

Concerning the maldistribution, the case $C2$ is with $\alpha = 0.468$, and it corresponds to the condition $\delta = 0$, so the imaginary projection of the guide vane toward the inlet splits the inflow into two equal parts. The flow distribution has improved with respect to the case $C1$, with an average value of $\varepsilon = 3.40\%$. The performance is even better for the case $C3$, with an average value of $\varepsilon = 0.70\%$, while for case $C4$ it becomes worst with $\varepsilon = 12.53\%$, with a larger flow in the channels 1 and 4 with respect to 2 and 3.

Figure 16 shows the analytical and the numerical results related to Eq. (14), i.e., the simplified model for the equal distribution condition. The solid line represents the right-hand side of Eq. (14), which is computed analytically as a function of α only. The triangle symbols are the results from the simulations $C1 - C4$, where the difference between the head loss coefficient

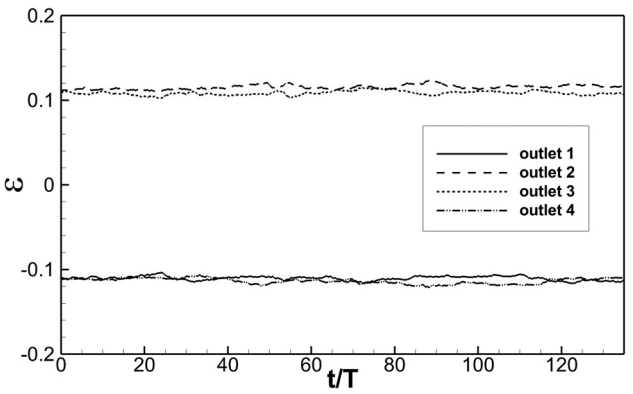

Fig. 14 Instantaneous maldistribution coefficient ε for the case *C*1 with $\alpha = 0.5$ for the outlets 1 to 4

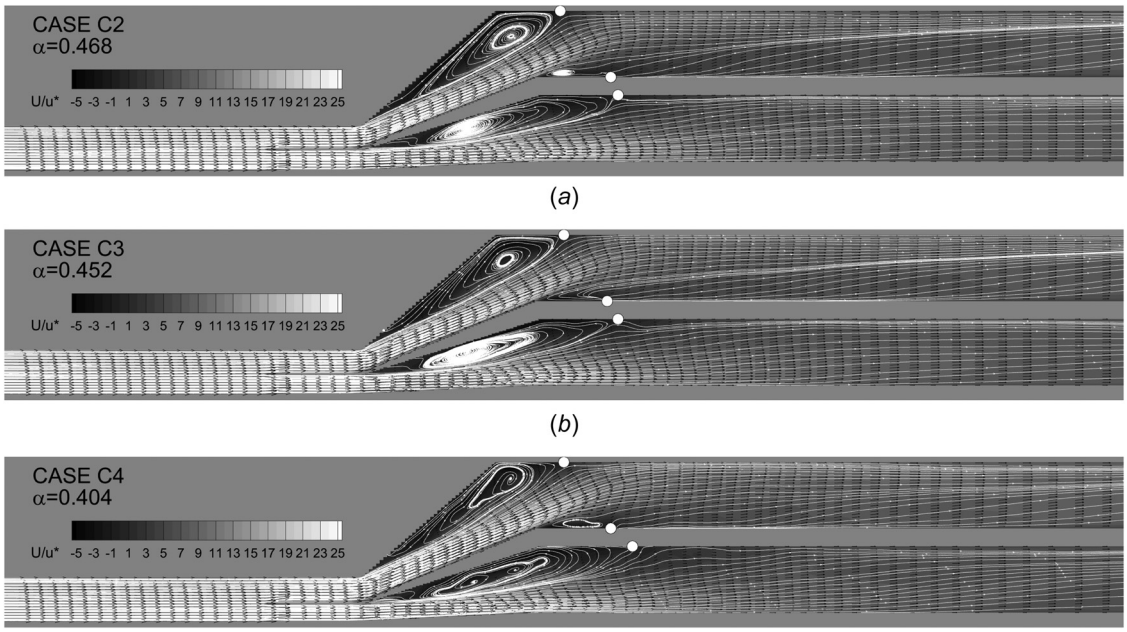

Fig. 15 Streamlines, velocity vectors, and contour for the mean streamwise velocity component *U*. The white circles correspond to the point with $\tau_{wall} = 0$: (*a*) case *C*2, (*b*) case *C*3, (*c*) case *C*4. For the sake of clarity only one vector every 16 is shown.

Table 3 Points of flow reattachment in terms of distance L/W_1 from the inlet

Case	Channel 1, 4	Channel 1, 4	Channel 2, 3
	outer wall	inner wall	outer wall
*C*1	6.32	6.81	6.88
*C*2	6.24	6.81	6.88
*C*3	6.28	6.76	6.88
*C*4	6.28	6.81	7.05

for the outlet channels have been computed and reported in the plot in terms of the left-hand side of Eq. (14). For the cases *C*1 and *C*2 the value of k_1 is greater than k_2 and therefore the LHS is positive, as α is further reduced, cases *C*3 and *C*4, the channels 1 and 4 have a greater flow rate with respect to the interior channels, and this behavior is associated with a value of k_1 lower than k_2, so the LHS values become negative. This behavior looks linear with α as it can be seen from the dashed line.

Together with the LHS and RHS computations, Fig. 16 reports also the modulus of ε values for the different cases. The simplified model indicates that an equal flow distribution can be obtained if Eq. (16) is satisfied, that is when the LHS is equal to the RHS. For $\alpha = 0.5$ and $\alpha = 0.404$ the flow rate deficit is of the order of 10%, while moving to intermediate value of α the flow rate deficit reduces suggesting the existence of a minimum as a function of α. In the view of these results, and to prove the effectiveness of the simplified model, an additional simulation is run, setting $\alpha = 0.462$, i.e., at the intersection between the RHS and LHS lines, for this case, a maldistribution of 1.23% is obtained. The minimum maldistribution is reached for $\alpha = 0.460$ (case C5), which corresponds to the intersection of LHS and RHS if V_x is set to half of the previous value in Eq. (13).

The behavior of ε for this last case is very close to zero, with an average value of $\varepsilon = 0.32\%$. Although a very good value is obtained, it has to be noticed that for this case, the expected value of the RHS should be -0.07, while numerically it is obtained -0.17, so it deviates from the previously supposed linear behavior. However, the condition of equal distribution looks satisfied.

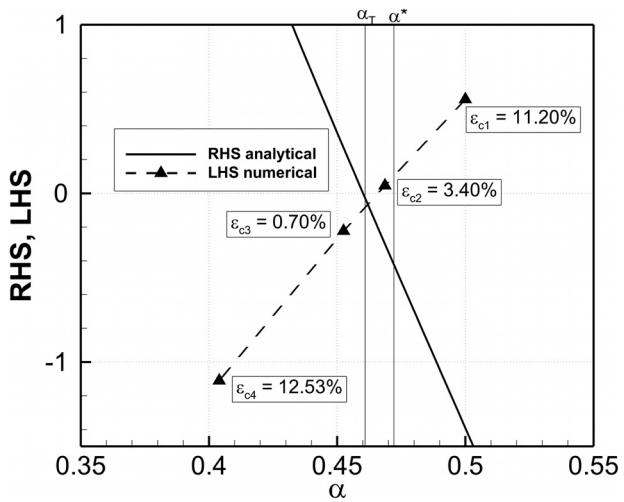

Fig. 16 Behavior of LHS and RHS of Eq. (14). Solid line the analytical RHS, Triangle and dashed line the LHS from simulation *C*1–*C*4.

Table 4 shows the maldistribution parameter averaged in time, for each outlet and for all the simulated cases with guide vanes. Statistically, few parts per thousand variations are observed. The values ε_{14} and ε_{23} report the mean value averaged between channels 1 and 4 and between 2 and 3 , respectively, they have opposite equal values as expected to satisfy the continuity equation. Finally, the values ε_{12} and ε_{34} report the summation of the maldistribution parameters with respect to the symmetry axis, showing a flow unbalance of few parts per thousand for all cases, except the optimized case *C*5, which has an order of magnitude less than the other cases.

Figure 17 shows the positions of eight lines on z direction along the x coordinate of the VM to evaluate the mean velocity profiles.

Figure 18 shows, for the above mentioned locations, the x component of the mean velocity U_m normalized by u_τ, the z coordinate has been normalized by the channel height $h(x, \alpha)$, which for each

Table 4 Maldistribution parameter across the channels

Case	ε_1	ε_2	ε_3	ε_4	ε_{14}	ε_{23}	ε_{12}	ε_{34}
$C1$	−0.1103	0.1155	0.1085	−0.1137	−0.112	0.112	0.0052	−0.0052
$C2$	−0.0317	0.0350	0.0327	0.0363	−0.034	0.034	0.0037	−0.0037
$C3$	0.0070	−0.0085	−0.0055	0.0070	0.007	−0.007	−0.0015	0.0015
$C4$	0.1287	−0.1243	−0.1263	0.1219	0.125	−0.125	−0.0044	0.0044
C5	−0.0008	0.0008	0.0060	0.0055	−0.003	0.003	0.0002	−0.0002

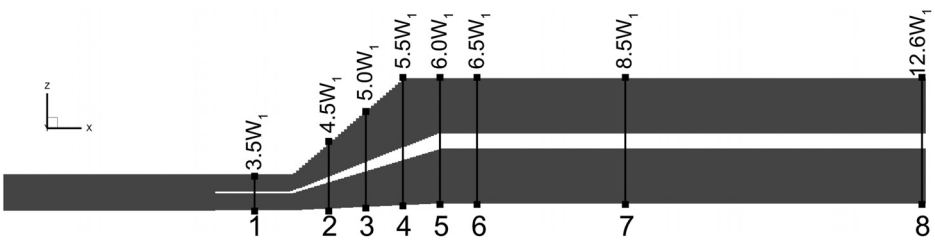

Fig. 17 Line data positions in the vertical manifolds

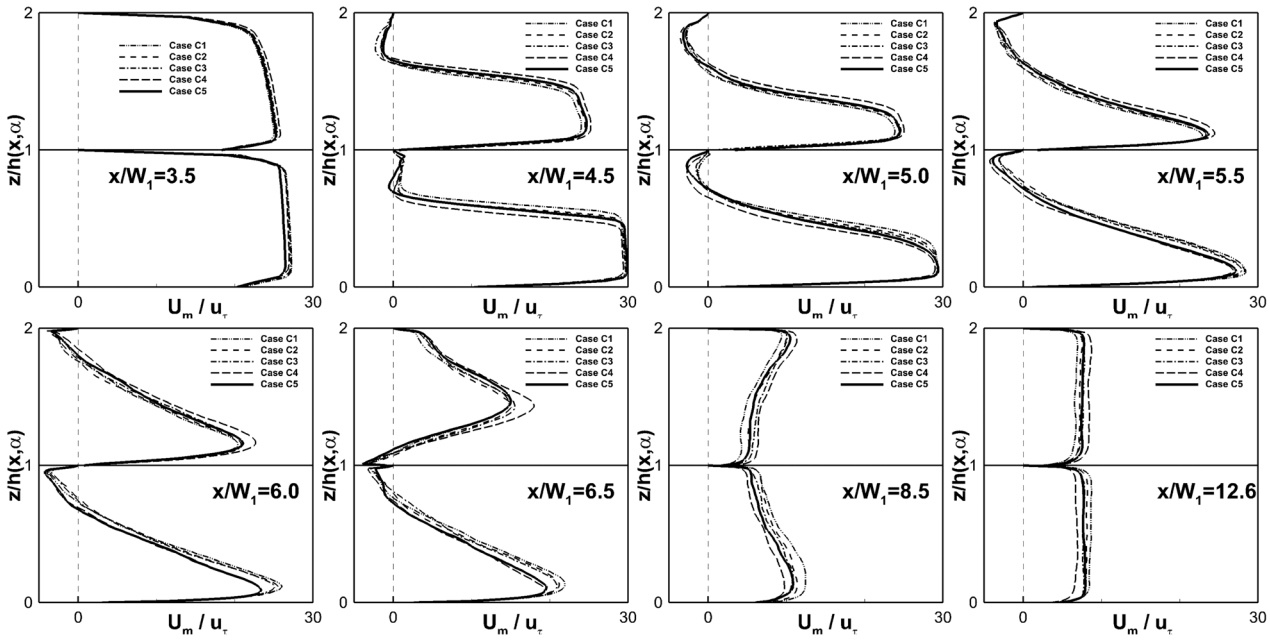

Fig. 18 Mean velocity *x* component profile along *z* direction, at 8 differents x-location for channel 1, top profile, and for channel 2, bottom profile

channel varies in terms of the x coordinate and of the guide vane position as a function of α. For each panel, the profile at the top refers to channel 1 (here the $z/h(x,\alpha)$ has been shifted by a quantity one), while the profile at the bottom refers to channel 2. The optimized case $C5$ is with a bold solid line, to highlight the differences with respect to the other cases. Therefore, the coordinate $z/h = 0, 1$ and $z/h = 1, 2$ correspond to the walls in the z direction for channel 2 and 1 , respectively.

The first location is at $x/W_1 = 3.5$, in the inlet duct within the guide vanes, the velocity profiles differ between the two channels, the flow enter the channel 1 with an already developed boundary layer, while at the walls $z/h = 0$ and $z/h = 1$ for channel 2, and $z/h = 1$ for channel 1 the boundary layer is still developing.

At the location $x/W_1 = 4.5$, channel 1 exhibits flow separation at the upper wall, while this behavior is not observed for channel 2, although some initial effect is visible close to the upper boundary.

Moving downstream, till $x/W_1 = 6.0$, flow separations are clearly identified for both the channels.

For all the cases, moving along the diffuser, from $x/W_1 = 4.5$ to $x/W_1 = 6.0$, the velocity gradient tends to reduce in the core of the two channels, between the through-flow region and the reverse flow region, probably, this is due to large scale mixing. Indeed, at $x/W_1 = 4.5$ a strong shear is observed, this shear allows the formation of Kelvin–Helmholtz billows, as they travel along the diffuser, they start to break, inducing turbulent mixing and the consequent effect on the velocity profile. For these locations, larger velocity is observed for the case $C4$ in the channel 1, and for the case $C1$ in the channel 2. The case $C5$ has lower velocity peaks with respect to the other cases, and in general it has an intermediate behavior with respect to the cases $C1$ and $C4$.

At the location $x/W_1 = 6.5$, the flow has reattached at the upper boundary for channel 1, but the velocity profile shows that a small flow separation area has developed at the bottom boundary, $z/h = 1$. For channel 2 the flow is not yet reattached.

The location $x/W_1 = 8.5$ is between the diffuser exit and the domain outlets, the velocity profiles are not symmetrical, for both

Table 5 Head loss coefficient k_0 referred to the inlet velocity for the entire manifolds system, k_1 and k_2 are the head loss coefficients from the guide vanes to the outlets, referred to the outlet velocity

Case	α	k_0	k_1	k_2
$C0$b	—	0.777	—	—
$C1$	0.500	0.841	8.02	5.51
$C2$	0.468	0.864	6.91	6.70
$C3$	0.452	0.867	6.35	7.36
$C4$	0.404	0.893	5.09	10.09
$C5$	0.460	0.880	6.73	7.51

channels 1 and 2, with a peak close to the upper boundary and to the bottom boundary , respectively. This behavior is related to the effect of the flow separation region at the diffuser exit for channel 2, while for channel 1 is related to the flow change direction between the diffuser and the outlet channel. A larger peak value is observed for the case $C4$ in the channel 1 and for the case $C1$ in channel 2, while the case $C5$ shows intermediate values and a smoother behavior.

At the exits, $x/W_1 = 12.6$, the velocity profile becomes uniform, because of the turbulent mixing. It can be observed that between the channel 1 and 2, for the case $C5$, the velocity profiles are very similar, while higher values are observed again for $C4$ in channel 1 and for $C1$ in channel 2, which is consistent with the analyzed maldistribution coefficient.

Table 5 shows the head loss coefficient for the system, considering both the local head loss due to the flow separation and the secondary flow and the continuous head loss due to friction. Overall the head loss coefficient k_0 (related to the inlet bulk velocity) for case $C0$ is a little bit lower than the cases with the guide vanes, and its value is in agreement with literature, $0.68 - 0.70$ by [27], and above 0.7 by [31]. The small discrepancy is probably due to the additional head loss related to the outlet channels. The guide vanes number adopted in the analyzed configurations is not the optimum number (six dividing walls), as suggested by literature, and they are not sufficient to avoid or at least to drastically reduce the flow separation at the inclined walls of the subdiffusers. Moreover, the subdiffuser configuration adds walls and therefore continuous loss for the flow, justifying the head loss results for the cases with guide vanes. Table 5 reports also the head loss coefficient, related to the outlet velocity, for the channels 1 and 2, after averaging with respect to the symmetry axis. These values show that the minimum maldistribution is not associated with the minimum value of $\Delta k = |k_1 - k_2|$, but to the configuration that has a Δk able to compensate the effect of the inlet velocity profile and of the momentum exchange before the guide vanes.

6 Conclusions

In the present work, the maldistribution of a VM has been analyzed both analytically and numerically with LES. The configuration was characterized by a wide planar diffuser and four outlets, with a varying position of the guide vanes spanning from the inlet to the outlet channels.

From a conceptual model of the system, a strategy to determine an equal flow distribution as a function of the guide vane position has been derived and then tested numerically. The results have shown that the use of guide vanes is very beneficial in terms of flow equal distribution, but also that it is very sensitive to the guide vane position. The configuration with an equal distance between the guide vane in the inlet channel, as suggested by literature, provides a maldistribution of 11.2%. Taking advantage of the analytical model, the maldistribution has been reduced to 0.32%, proving the quality of the method.

The proposed method can be useful for the design procedure to reduce man hours and computational cost, minimizing the number of simulations required to obtain a configuration with the best performance in terms of maldistribution. For example, a trend for the head loss difference between the channels (LHS of Eq. (14)) can be determined with three simulations, then the optimum configuration can be found from the intersection with the RHS of Eq. (14). The method can be easily adapted to the case of disturbed inlet velocity profile, for example, downstream a fan or a bend, simply introducing a different expression for $\delta(\alpha)$ in the Eq. (13). Morover, the method can be used also in the framework of anular diffuser, for this case the assumption that the wall stress in the spanwise direction (read angular direction) is negligible, is not necessary. In general, f m the experimental result it can be useful for flow partitioning in hydraulic systems.

References

[1] Ibrahim, H., Ahmed, W., Abdou, S., and Blagojevic, V., 2018, "Experimental and Numerical Investigations of Flow Through Catalytic Converters," Int. J. Heat Mass Transfer, **127**, pp. 546–560.

[2] Park, N., Yoon, S., Jeong, W., and Jeong, Y., 2021, "A Study on the Evaluation of Flow Distribution Evenness in Parallel-Arrayed-Type Low-Pressure Membrane Module Piping," Membranes, **11**(10), p. 751.

[3] You, Y., Wu, Z., Liu, H., Zhang, A., Zeng, X., and Shen, X., 2018, "A Flexible Hybrid Cfd Model for Refrigeran Mal-Distribution Among Minichannels in Parallel Flow Condensers," Int. J. Refrig., **91**, pp. 80–88.

[4] Basu, S., Wang, C., and Chen, K., 2010, "Analytical Model of Flow Distribution in Polymer Electrolyte Fuel Cell Channels," Chem. Eng. Sci., **65**(23), pp. 6145–6154.

[5] Dammalapati, S., Aghalayam, P., and Kaisare, N., 2021, "Modeling the Effects of the Inlet Manifold Design on the Performance of a Diesel Oxidation Catalytic Converter," Ind. Eng. Chem. Res., **60**(10), pp. 3860–3870.

[6] Garcia-Guendulain, J., Riesco-Avila, J., Elizalde-Blancas, F., Belman-Flores, J., and Serrano-Arellano, J., 2018, "Numerical Study on the Effect of Distribution Plates in the Manifolds on the Flow Distribution and Thermal Performance of a Flat Plate Solar Collectors," Energies, **11**(5), p. 1077.

[7] Kline, S., Abbott, D., and Fox, R., 1959, "Optimum Design of Straight-Walled Diffusers," ASME J. Basic Eng., **81**(3), pp. 321–329.

[8] Bajura, R., 1971, "A Model for Flow Distribution in Manifolds," J. Eng. Power, **93**(1), pp. 7–12.

[9] Bajura, R., and Jones, E., 1976, "Flow Distribution Manifolds," ASME J. Fluids Eng., **98**(4), pp. 654–665.

[10] Shen, P., 1992, "The Effect of Friction on Flow Distribution in Dividing and Combining Manifolds," ASME J. Fluids Eng., **114**(1), pp. 121–123.

[11] Zhengqing, M., and Tongmo, X., 2006, "Single Phase Flow Characteristics in the Headers and Connecting Tube Parallel Tube Platen Systems," Appl. Therm. Eng., **26**(4), pp. 396–402.

[12] Zhang, W., Li, A., Gao, R., and Li, C., 2018, "Effects of Geometric Structures on Flow Uniformity and Pressure Drop in Dividing Manifold System With Parallel Pipe Array," Int. J. Heat Mass Transfer, **127**, pp. 870–881.

[13] Chen, A., and Sparrow, E., 2009, "Turbulence Modeling for Flow in a Distribution Manifold," Int. J. Heat Mass Transfer, **52**(5–6), pp. 1573–1581.

[14] Wang, J., 2011, "Theory of Flow Distribution in Manifolds," Chem. Eng. J., **168**(3), pp. 1331–1345.

[15] Dąbrowski, P., and Kumar, R., 2021, "Minichannel and Minigap Classification Criteria Based on the Aspect Ratio of the Minigeometry: A Numerical Study," Int. Commun. Heat Mass Transfer, **129**, p. 105685.

[16] Liu, H., and Li, P., 2013, "Even Distribution/Dividing of Single Phase Fluids by Symmetric Bifurcation on Flow Channels," Int. J. Heat Fluid Flow, **40**, pp. 165–179.

[17] Mazur, M., Bhatelia, T., Kuan, B., Patel, J., Webley, P. A., Brandt, M., Pareek, V., and Utikar, R., 2019, "Additively Manufactured, Highly-Uniform Flow Distributor for Process Intensification," Chem. Eng. Process.: Process Intensif., **143**, p. 107595.

[18] Porter, S., Saul, J., Aleksandrova, S., Medina, H., and Benjamin, S., 2016, "Hybrid Flow Modelling Approach Applied to Automotive Catalysts," Appl. Math. Model., **40**(19–20), pp. 8435–8445.

[19] Rebrov, E., Ismagilov, I., Ekatpure, R., Croon, M. D., and Schouten, J., 2007, "Header Design for Flow Equalization in Microstructured Reactors," AIChE J., **53**(1), pp. 28–38.

[20] Zhang, Z., and Li, Y., 2003, "Cfd Simulation on Inlet Configuration of Plate-Fin Heat Exchangers," Cryogenics, **43**(12), pp. 673–678.

[21] Belvin, R., 1984, *Applied Fluid Dynamics Handbook*, Reinhold Co., Van Nostrand, New York.

[22] Reneau, L., Johnston, J., and Kline, S., 1967, "Performance and Design of Straight, Two-Dimensional Diffuser," J. Basic Eng., **89**(1), pp. 141–150.

[23] Klugmann, M., Dabrowski, P., and Mikielewicz, D., 2018, "Pressure Drop Related to Flow Maldistribution in a Model Minichannel Plate Heat Exchanger," Arch. Thermodyn., **39**(2), pp. 123–146.

[24] Sahin, B., and Ward-Smith, A., 1987, "The Use of Perforated Plates to Control the Flow Emerging From a Wide-Angle Diffuser, With Application to Electrostatic Precipitator Design," Int. J. Heat Fluid Flow, **8**(2), pp. 124–131.

[25] Barratt, D., and Kim, T., 2015, "A Banked Wide-Angle Diffuser With Application to Electrostatic Precipitators," J. Power Energy, **229**(1), pp. 88–98.

[26] Kim, D., Jeong, S., Kim, J., and Lee, S., 2021, "Structure and Arrangement of Perforated Plates for Uniform Flow Distribution in an Electrostatic Precipitator," J. Air Waste Manage. Assoc., **71**(3), pp. 328–338.

[27] Idelchik, I., 2007, *Handbook of Hydraulic Resistance*, Begell House, inc., New York.
[28] Mariotti, A., Buresti, G., and Salvetti, M., 2014, "Control of the Turbulent Flow in a Plane Diffuser Through Optimized Contoured Cavities," Eur. J. Mech. B/ Fluids, **48**, pp. 254–265.
[29] Yang, J., Zhang, Y., Chen, H., and Fu, S., 2020, "Unsteady Flow Control of a Plane Diffuser Based on a Karman-Vortex Generator," AIP Adv., **10**(5), p. 055314.
[30] Dabrowski, P., 2020, "Mitigation of Flow Maldistribution in Minichannel and Minigap Heat Exchanger by Introducing Threshold in Manifolds," J. Appl. Fluid Mech., **13**(3), pp. 815–826.
[31] Miller, D., 1978, *Internal Flow Systems*, BHRA Fluid Engineering, Bedfordshire, UK.
[32] Piomelli, U., and Balaras, E., 2002, "Wall-Layer Models for Large-Eddy Simulations," Annu. Rev. Fluid Mech., **34**(1), pp. 349–374.
[33] Kaltenbach, H., Fatica, M., Mittal, R., Lund, T., and Moin, P., 1999, "Study of Flow in a Planar Asymmetric Diffuser Using Large-Eddy Simulation," J. Fluid Mech., **390**, pp. 151–185.
[34] Iaccarino, G., 2001, "Prediction of a Turbulent Separated Flow Using Commercial Cfd Codes," ASME J. Fluids Eng., **123**(4), pp. 819–828.
[35] Kim, J., Shin, J., Sohn, S., and Yoon, S., 2019, "Analysis of Non-Uniform Flow Distribution in Parallel Micro-Channels," J. Mech. Sci. Technol., **33**(8), pp. 3859–3864.
[36] Zang, Y., Street, R., and Koseff, J., 1994, "A Non-Staggered Grid, Fractional Step Method for Time-Dependent Incompressible Navier-Stokes Equations in Curvilinear Coordinates," J. Comput. Phys., **114**(1), pp. 18–33.
[37] Alves, M., Oliveira, P., and Pinho, F., 2003, "A Convergent and Universally Bounded Interpolation Scheme for the Treatment of Advection," Int. J. Numer. Methods Fluids, **41**(1), pp. 47–75.
[38] Fadlun, E., Verzicco, R., Orlandi, P., and Mohd-Yusof, J., 2000, "Combined Immersed-Boundary Finite Difference Methods for Three-Dimensional Complex Flow Simulations," J. Comput. Phys., **161**(1), pp. 35–60.
[39] Roman, F., Napoli, E., Milici, B., and Armenio, V., 2009, "An Improved Immersed Boundary Method for Curvilinear Grids," Comput. Fluids, **38**(8), pp. 1510–1527.
[40] Mittal, R., and Iaccarino, G., 2005, "Immersed Boundary Methods," Annu. Rev. Fluid Mech., **37**(1), pp. 239–261.
[41] Bose, S., and Park, G., 2018, "Wall-Modeled Large-Eddy Simulation for Complex Turbulent Flows," Annu. Rev. Fluid Mech., **50**(1), pp. 535–561.
[42] Kaltenbach, H., 1997, "Cell Aspect Ratio Dependence of Anisotropy Measures for Resolved and Subgrid Scale Stresses," J. Comput. Phys., **136**(2), pp. 399–410.
[43] Cabot, W., and Moin, P., 2000, "Approximate Wall Boundary Conditions in the Large-Eddy Simulation of High Reynolds Number Flow," Flow Turbul. Combust., **63**(1/4), pp. 269–291.
[44] Nicoud, F., Bagget, J., Moin, O., and Cabot, W., 2001, "Large Eddy Simulation Wall-Model Based on Suboptimal Control Theory and Linear Stochastic Estimation," Phys. Fluids, **13**(10), pp. 2968–2984.
[45] Roman, F., Armenio, V., and Fröhlich, J., 2009, "A Simple Wall-Layer Model for Large Eddy Simulation With Immersed Boundary Methode," Phys. Fluids, **21**(10), p. 101701.
[46] Blanchard, S., Odier, N., Gicquel, L., Cuenot, B., and Nicoud, F., 2021, "Stochastic Forcing for Sub-Grid Scale Models in Wall-Modeled Large-Eddy Simulation," Phys. Fluids, **33**(9), p. 095123.
[47] Piomelli, U., 2008, "Wall-Layer Models for Large-Eddy Simulations," Prog. Aerosp. Sci., **44**(6), pp. 437–446.
[48] Brundrett, E., and Baines, W., 1964, "The Production and Diffusion of Vorticity in Duct Flow," J. Fluid Mech., **19**(3), pp. 375–394.
[49] Orlanski, I., 1976, "A Simple Boundary Condition for Unbounded Hyperbolic Flows," J. Comput. Phys., **21**(3), pp. 251–269.
[50] Chang, P., 1970, *Separation of Flow*, Pergamon Press, Oxford, UK.
[51] Herbst, A., Schlatter, P., and Henningson, D., 2007, "Simulation of Turbulent Flow in a Plane Asymmetric Diffuser," Flow Turbul. Combust., **79**(3), pp. 275–306.
[52] Lan, H., Armaly, B., and Drallmeier, J., 2009, "Turbulent Forced Convection in a Plane Asymmetric Diffuser: Effect of Diffuser Angle," ASME J. Heat Transfer, **131**(7), p. 071702.